Highly Conductive Ceramic-in-Polymer Composite Electrolyte Enabling Superior Electrochemical Performance for All-Solid-State Lithium Batteries

Asish Kumar Das, Manish Badole, Hari Narayanan Vasavan, Samriddhi Saxena, Pratiksha Gami, Sunil Kumar*

Department of Metallurgy Engineering and Materials Science, Indian Institute of Technology Indore, Simrol, 453552, India

*Corresponding author E-mail: sunil@iiti.ac.in

Abstract: In the present work, poly (vinylidene fluoride-co-hexafluoropropylene) [P(VDF-HFP)] and various amounts of NASICON-type $LiZr_{1.5}Sn_{0.5}(PO_4)_3$ (LZSP) as the active filler were used to fabricate composite solid electrolytes (CSEs) by solution-casting method and their structural and electrochemical behaviour were studied. The X-ray diffraction (XRD) data showed the compatibility of the rhombohedral LZSP with P(VDF-HFP). A uniform distribution of ceramic particles in the polymer was observed from scanning electron microscopy (SEM) images and energy X-ray dispersive maps. The addition of 15% wt. ceramic filler to the polymer matrix enhanced the room temperature ionic conductivity ($\sigma \sim 2.87 \times 10^{-5}$ S/cm), lithium-ion transference number ($t_{Li^+} \sim 0.55$), and electrochemical stability window (~ 4.87 V). The reversibility and endurance of lithium-ion conduction across the composite electrolyte at various current densities were confirmed through galvanostatic charge-discharge measurements on a symmetric lithium cell for more than 500 h. A full cell fabricated using a commercial grade $LiMn_2O_4$ cathode and the optimised CSE electrolyte showed excellent rate performance at room temperature. The cell delivered a discharge capacity of 105 mAh/g with a nominal voltage of 4.0 V and retained 93% of its initial capacity after 100 cycles at a current density of 0.1 mA/cm^2.

Keywords: NASICON; Composite solid electrolytes; Ionic conductivity; Transference number; All-solid-state cell.

1. Introduction

The ever-increasing oil price, global warming, and depletion of fossil fuels led to green technologies using renewable energy sources and an increased focus on efficient energy storage systems. The current energy storage technologies require significant development to meet the demand for continuous energy supply. Lithium battery technology has superior energy density and excellent cycling life compared to various energy storage technologies [1-4]. This enables them to be used extensively in portable electronic devices like mobile phones, laptops, smartwatches, etc. [3, 5, 6]. However, the technology still needs to improve to attain the required energy density and charging capabilities for application in electric vehicles and other portable devices [7-10]. It is important to note that using high-voltage cathodes and high specific capacity anodes, such as lithium metal, in conventional lithium-ion batteries could help to realise high energy density batteries needed for electric vehicles and other applications [10-12]. A significant hurdle in achieving these goals is the continuous formation of solid electrolyte interphase (SEI) in lithium metal which causes drastic degradation in the performance of the lithium battery. There is also a major safety concern associated with the incapability of liquid electrolytes to suppress the growth of dendritic lithium. To overcome these challenges, it is necessary to replace liquid electrolytes with non-flammable solid electrolytes.

Solid electrolytes are typically categorised into inorganic ceramic and organic polymer electrolytes [13, 14]. Among inorganic solid electrolytes, sulfide-based electrolytes like thio-LISICON and Argyrodites show room temperature ionic conductivity $\geq 10^{-2}$ S/cm [15]. However, the narrow electrochemical window and high moisture sensitivity hinder their application in all-solid-state lithium batteries. On the other hand, oxide-based solid electrolytes offer a decent room temperature ionic conductivity ($\geq 10^{-4}$ S/cm), wide electrochemical window (> 4 V), better chemical stability with electrodes, and less moisture sensitivity [16-

18]. Various research efforts have been focused on enhancing the ionic conductivity of NASICON type [$LiM_2(PO_4)_3$] electrolytes either by increasing the bottleneck size of the Li^+ transport or the lithium concentration in the unit cell [19]. Isovalent substituents like Sn^{4+}, Hf^{4+}, etc., help in improving the easy migration of lithium-ion in the unit cell, whereas aliovalent substitution by Al^{3+}, Sr^{2+}, Sc^{3+}, Y^{3+}, Mg^{2+}, La^{3+}, and Ca^{2+} increase the lithium-ion concentration in the unit cell [16, 20-30]. Despite these properties, ceramic electrolytes struggle to find a place in commercial applications due to their brittle nature, large interfacial resistance with the electrodes, and high manufacturing cost.

Solid polymer electrolytes exhibit better interfacial compatibility with the electrodes owing to their flexible nature, lightweight, and low processibility cost compared to the inorganic solid ceramic electrolytes. In solid-state batteries, various polymers like Poly (ethylene oxide) [PEO], Polyacrylonitrile [PAN], Poly (methyl methacrylate) [PMMA], Poly (vinylidene fluoride) [PVDF], Poly (vinylidene fluoride-hexafluoro propylene) [P(VDF-HFP)], Poly (vinyl chloride) [PVC], Poly (vinyl alcohol) [PVA], Poly (dimethylsiloxane), Polycarbonate, etc. are complexed with various concentrations of lithium salts like $LiPF_6$, $LiBF_4$, LiTFSI, $LiClO_4$, $LiAsF_6$, LiBOB, etc. [31-40]. However, a low lithium ion conductivity (< 10^{-5} S/cm) limits their scope in all-solid-state lithium batteries [41]. These issues of polymer electrolytes can be addressed by altering the techniques such as solvent-free crosslinking, blending, in-situ photo-polymerisation, plasticisation, and incorporation of inorganic fillers [41, 42]. Many reports showed improvement in the ionic conductivity of composite polymers due to the dispersion of passive inorganic fillers, such as SiO_2, TiO_2, Al_2O_3, WO_3 etc. [43-46]. Passive fillers act as plasticisers to transform the crystalline phase to the amorphous phase in polymer and could help in the dissociation of salt by Lewis acid-base interaction [47]. Active fillers such as $Li_{0.5}La_{0.5}TiO_3$ (LLTO), LLZO ($Li_7La_3Zr_2O_{12}$), $Li_{1.5}Al_{0.5}Ge_{1.5}(PO_4)_3$ (LAGP), $Li_{6.7}La_3Zr_{1.7}V_{0.3}O_{12}$, $Li_{1.3}Al_{0.3}Ti_{1.7}(PO_4)_3$ (LATP), $LiSnZr(PO_4)_3$ (LSZP),

$Li_{6.25}La_3Sn_{1.25}Bi_{0.75}O_{12}$, $LiAlO_2$ (LAO), etc., on the other hand, provide more lithium-ion conduction path in the composite electrolyte enabling the composite polymer electrolytes to leverage the properties of both ceramics and polymers [16, 41, 48-59]. Ceramic electrolytes provide high ionic conductivity and good mechanical strength, whereas polymer electrolytes have low interfacial resistance with electrodes and high elasticity. Fan et al. have achieved interfacial resistance of ~ 3767 Ω in a symmetric lithium cell upon dispersion of a Ga and Nb co-doped garnet (LGLZNO) in PEO polymer [60]. A PVDF-based composite electrolyte fabricated by Yu et al. with $Li_{10}GeP_2S_{12}$ (LGPS) as the ceramics filler resulted in a high ionic conductivity of ~ 2.64×10^{-4} S/cm at 50 °C [61]. Another study by Seol et al. showed an ionic conductivity of 1.2×10^{-5} S/cm for the composite electrolyte (LLZO/PVDF-HFP/LiTFSI) [62].

In this study, powders of NASICON type $LiZr_{1.5}Sn_{0.5}(PO_4)_3$ as fillers in P(VDF-HFP)-LiTFSI salt matrix were used to fabricate composite solid electrolytes (CSE). The NASICON type LZSP showed the bulk conductivity of the order of ~ 10^{-3} S/m. P(VDF-HFP) is selected as the polymer due to its high capacity for salt dissolution and simplicity in the fabrication of the free-standing film. LiTFSI is chosen as the salt for its excellent complexation with the P(VDF-HFP) and restricted anionic movement due to heavier $TFSI^-$. Improved ionic conductivity is observed in the modified polymer electrolyte upon adding LZSP, which provides more lithium-ion transport channels. The dispersed ceramic particles are intended to provide the mechanical strength to resist the dendrite growth and thermal stability of the polymer electrolyte. The electrochemical behaviour of solid-state cells fabricated employing the composite electrolyte with 15% ceramic content, lithium metal anode, and spinel type $LiMn_2O_4$ cathode is reported.

2. Experimental Section

2.1. Synthesis of LZSP

The solid-state reaction method was used to synthesise the desired composition $LiZr_{1.5}Sn_{0.5}(PO_4)_3$, stoichiometric amounts of lithium carbonate (Li_2CO_3), tin (IV) oxide (SnO_2), zirconium oxychloride octahydrate ($ZrOCl_2 \cdot 8H_2O$), and ammonium dihydrogen phosphate ($NH_4 \cdot H_2PO_4$) (purity > 99%) were taken with an additional 10% of lithium precursor to compensate for lithium volatilisation at higher synthesis temperatures. The precursors were first mixed in the mortar pestle for 30 minutes, followed by ball-milling in ethanol for 12 h. The mixture was heated at 550 °C for 12 h, then at 750 °C for 12 h. The powder was pressed into cylindrical pellets with a diameter of ~ 10 mm and thickness of ~ 1 mm by applying a uniaxial pressure of 200 MPa in a hydraulic press. These green pellets were sintered at 1150 °C for 12 h after covering them with the same powder to minimise the lithium loss.

2.2. Fabrication of Composite Solid Electrolyte

P(VDF-HFP) pellets (average M_w~ 400,000) (Sigma Aldrich), LiTFSI (purity >99.0%, Alfa Aesar), and *N, N*-Dimethylformamide (DMF) (purity > 99.9%, Sigma Aldrich) and the ball-milled powder of sintered LZSP pellet were used in different weight ratios to prepare the composite solid electrolyte films by solution casting method. The weighed P(VDF-HFP) pellets are dissolved in organic DMF solvent under continuous stirring to prepare a transparent solution into which the LiTFSI salt in the desired ratio is added [P(VDF-HFP): LiTFSI ~ 2.5 gm:1 gm]. After ultrasonication of the ball-milled LZSP powder in DMF solvent, it was dispersed in the stirred polymeric salt solution in different wt. percentages 0%, 5%, 10%, 15%, and 20% (henceforth referred to as CSE-0, CSE-5, CSE-10, CSE-15, and CSE-20 regarding the percentage of LZSP in polymer-salt). The mixture was stirred at room temperature to make the solution homogeneous and viscous enough for casting on a Petri dish, followed by placing the petri dish in a vacuum oven at 50 °C for 36 h to evaporate the solvent. The CSE films, peeled off from the Petri dishes, are kept in an argon-filled glove box for further experimental procedures.

2.3. Fabrication of coin cells

18 mm diameter punched CSE -15 membrane was used to prepare symmetric cell (Li| CSE -15|Li), asymmetric cell (Li| CSE -15|SS), and full cell (Li| CSE -15|$LiMn_2O_4$), where $LiMn_2O_4$ (LMO) was bought from MTI corporation (specific capacity ~ 110 mAh/g, single side coated on an aluminium foil with active material density ~ 16.6 mg/cm^2) (XRD pattern of LMO is shown in Fig. S1). During the fabrication of Li|CSE-15|$LiMn_2O_4$ cell, a 5 μL of 1 M $LiPF_6$ in EC: DMC was dropped on the cathode sheet to improve the interfacial conduction between cathode and composite solid electrolyte.

2.4. Characterisations

X-ray diffraction (XRD) technique was used to confirm the phase of ceramic $LiZr_{1.5}Sn_{0.5}(PO_4)_3$, polymer-salt complex, and composite membranes. Empyrean (Malvern Panalytical) x-ray diffractometer (operating condition: 40 kV, 200 mA) with Cu-K_α radiation in the 2θ range from 10° to 70° (a step size of ~ 0.01°) to obtain the XRD data of the samples. JSM field emission scanning microscope (FESEM, model JEOL-7610+) was used to confirm the microstructure and elemental distributions of composite electrolyte membranes. A Perkin Elmer Spectrum IR (Model number: Spectrum 2) was operated to obtain the Fourier Transform Infrared (FTIR) transmittance spectra ranging from 400 cm^{-1} to 2200 cm^{-1}. Differential scanning calorimetry (Netzsch DSC 214 Polyma) was employed for the thermal analysis of CSE-0 and CSE-20 samples with a scan rate of 5 ºC/min and flowing N_2 environment. The mechanical properties of CSE-0 and CSE-15 with a cross-sectional area of 0.50 mm^2 and a gauge length of 10 mm at 25 ºC were obtained using a universal testing machine (UTM) with a tensile loading speed of 5 mm/min. The complex impedance measurements on sintered LZSP pellet (silver electroded on either side) and CSEs sandwiched between two symmetric electrodes (lithium metal or stainless steel) were carried out in 1 Hz to 1 MHz frequency range using the NF (Model: ZM2376) LCR meter by applying a signal of 100 mV. For temperature-dependent impedance measurements, a cryogenic set-up with Lake Shore cryotronics was used to vary the sample temperature. Keithley Source Meter Unit (model 2450-EC) was used to perform cyclic voltammetry (CV) & DC polarisation measurements in the symmetric cell with lithium metal foil as non-blocking electrodes and linear sweep voltammetry (LSV) on the asymmetric cell with lithium metal as the non-blocking electrode & stainless steel as the ion-blocking electrode at room temperature (25 ºC). The galvanostatic charge-discharge (GCD) measurements on symmetric lithium cells employing CSEs were carried out at room temperature to confirm the reversibility and endurance of lithium-ion conduction across the composite membranes at various current densities. Room-temperature (25 ºC) GCD tests were also performed on coin cells (CR 2032) fabricated inside an argon-filled glovebox employing the optimized composite CSE-15 as the electrolyte, $LiMn_2O_4$ as the working electrode, and lithium metal as the counter and reference electrode.

3. Results and discussions

3.1. XRD analysis

Figure 1(a) shows the experimental room temperature XRD pattern of LZSP powder calcined at 1150 °C along with the Rietveld refinement profile and difference curve. The Rietveld refinement was carried out using the software TOPAS Academic (version 6) [63]. The peak profile was refined using the pseudo-Voigt function with an asymmetry correction according to axial divergence, and an 8-order polynomial function was used to fit the background. Sample displacement error and lattice parameters were varied during the refinement. The lattice parameters were found to be $a = b = 8.8039(4)$ Å & $c = 22.0007(3)$ Å, and a volume of 1476.78(9) Å^3. The refined parameters of LZSP are given in Table 1. All peaks in the XRD pattern match well with the rhombohedral structure (S.G: $R\bar{3}c$). The rhombohedral structure of LZSP is found to be stable at a lower calcination temperature of 1150 °C when compared to the rhombohedral $LiZr_2(PO_4)_3$ (LZP), as reported earlier due to the effect of the isovalent substitution of Zr^{4+} (ionic radii in octahedral coordination = 0.65Å) by Sn^{4+} (ionic radii in octahedral coordination = 0.72 Å) [20, 64].

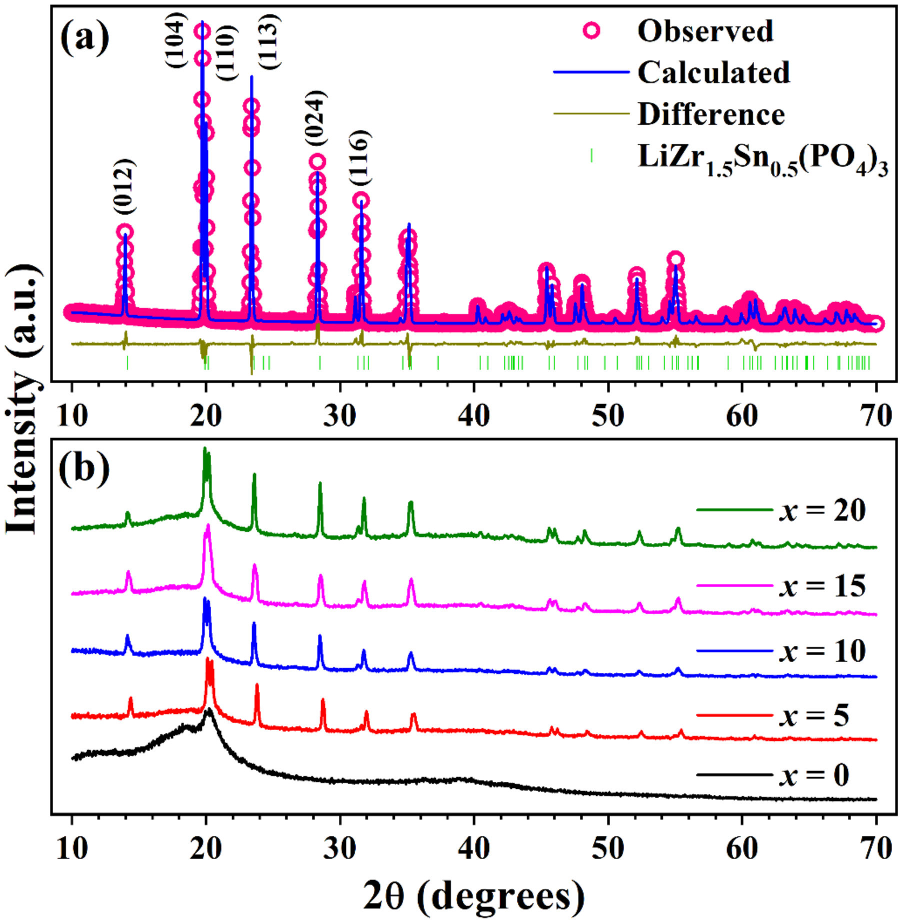

Fig. 1. *(a) Powder x-ray diffraction data (open circles) for LZSP sample sintered at 1150 °C for 12 h. The calculated pattern obtained from the refinement is shown as a thick blue line; the profile difference is depicted with a thin khaki line. The calculated Bragg positions are shown by vertical bars at the bottom, (b) x-ray diffraction patterns of CSE-x (x = 0, 5, 10, 15, and 20).*

Further, it is believed that lithium-ion migrates mostly through Li1 (6b positions), Li2 (18e position), and Li3 (36f position). The activation energy is determined by the bottleneck size for lithium-ion transport in the rhombohedral structure formed by three oxygen atoms. In the case of isovalent substitution of Zr^{4+} by Sn^{4+} in $LiZr_{1.5}Sn_{0.5}(PO_4)_3$ (LZSP), the Li-O_6 polyhedral volume (16.3311 $Å^3$) is larger than reported for $LiSn_2(PO_4)_3$ (LSP, 14.479 $Å^3$) and the bond valence sum for Li1 in LZSP was calculated to be 0.428 using the VESTA software (with bond valence parameter ~ 1.466) which is lower than the Li1 in LSP (0.565) [16, 65, 66]. Further, there is an increase in electronegativity at the M-site owing to the substitution of 25% Sn^{4+} (electronegativity of Zr = 1.33 and Sn = 1.96 on the Pauling scale), which is expected to weaken the Li-O bond strength in LZSP as compared to $LiZr_2(PO_4)_3$. There is an interplay between these factors resulting in higher ionic conductivity in comparison with LZP and LSP. The lithium-ion conduction in rhombohedral NASICON-type structure is *via* the 3D connected tunnels. To visualize the Li-ion migration path through the LZSP crystal structure, the cif file obtained from the Rietveld refinement of XRD data was utilized in softBV software developed by Chen and Adams [67-69]. The output of BVPA software was used in the VESTA software and the result is shown in Fig. S2. The figure confirms the three-dimensionally connected Li-ion migration pathways in rhombohedral LZSP.

The compatibility of LZSP as ceramic filler with the polymer P(VDF-HFP) was assessed by analysing XRD patterns of composite films as shown in Fig. 1(b). For CSE-0, a small broad peak around ~ 20° indicates the existence of semi-crystallinity corresponding to the α-phase of P(VDF-HFP) [70, 71]. For CSE-5, the rhombohedral LZSP phase peaks appear in the XRD patterns, these peaks become prominent with the increase in the ceramic filler content. No change in XRD peaks corresponding to the $R\overline{3}c$ phase of LZSP signifies the compatibility of LZSP filler and P(VDF-HFP) polymer matrix.

3.2. Microstructure analysis

The scanning electron microscopy (SEM) images and energy dispersive spectroscopy (EDS) data of the representative CSE-15 electrolyte membrane are shown in Fig. 2(a-j). In the CSE-15 electrolyte membrane, the polymer chains were well connected by the dispersed LZSP particles, which facilitates the lithium-ion conduction in the solid electrolyte lowering the activation energy. The filler consisting of the elements Zr, Sn, P, and O is uniformly distributed in the polymer-salt matrix (Fig. 2(b)). The SEM image of CSE-0 is provided in Fig. S3, and the SEM images of the surface and cross-section of CSE-20 are given in Figs. S4 and S5, respectively, in the Supplementary Materials. The agglomeration of LZSP particles is observed in the CSE-20 membrane, which hinders the facile lithium-ion conduction in the composite electrolyte. On the other hand, polymer chains are not well connected in CSE-0 electrolyte film, contributing to higher activation energy as compared to composite with ceramic filler.

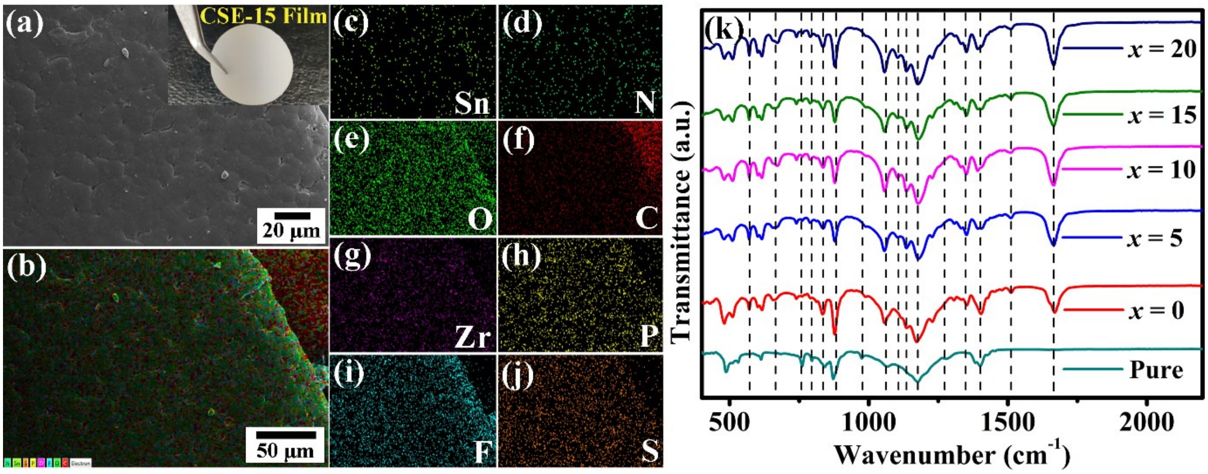

Fig. 2. *(a) Scanning electron microscopy (SEM) image of CSE-15, (b)-(j) Energy dispersive spectroscopy (EDS) data of CSE-15 along with its constituent elemental distributions, (k) Fourier transform infrared spectroscopy of pure P(VDF-HFP) and CSE-x (x = 0, 5, 10, 15, and 20) (Inset Fig. 2(a) shows the photograph of CSE-15 film).*

3.3. FTIR Spectroscopy

The effect of salt and ceramic filler on the structure and molecular bonds (IR active) in the P(VDF-HFP) polymer matrix was analyzed by FTIR spectroscopy, and the spectra are given in Fig. 2(k). The change in the FTIR absorbance spectra ranged from 400 cm^{-1} - 2200

cm^{-1} upon the addition of LiTFSI salt and ceramic filler in different fractions. The absorbance peaks around 761, 794, 840, 875, 975, 1178, 1278, and 1400 cm^{-1} can be assigned to -CH_2 rocking vibrations, -CF_3 stretching vibrations, a mixed mode of -CH_2 rocking, combined -C-C-vibrations and -CF_2 symmetric stretching, C-F stretching vibrations, C-F symmetric stretching vibrations, -CF_3 symmetric stretching vibrations, and -CH_2 wagging, respectively of pure P(VDF-HFP) [62, 72, 73]. Four additional peaks about 1668, 1510, 1058, and 571 cm^{-1} were observed in the FTIR spectrum of CSE-0. The peaks about 1058 and 571 cm^{-1} are due to the asymmetric -S-N-S- stretching of LiTFSI and asymmetric -CF_3 bending vibrations of LiTFSI salt, respectively [62, 72]. The peak at 1510 cm^{-1} is attributed to the C=C stretching vibration, which was observed upon the addition of lithium salt. C=C is generated upon the addition of lithium salt, which causes dehydrofluorination in the *vinylidene fluoride* (-CH_2-CF_2-) of P(VDF-HFP) leading to the conversion of -CH_2-CF_2- to -CH=CF- in the presence of DMF. The incorporation of LZSP ceramic particles also increases the alkaline environment which further aids in the dehydrofluorination of *vinylidene fluoride* [74]. The peak at 1668 cm^{-1} is attributed to the dissociation and complexation of LiTFSI in the polymer matrix. The addition of LiTFSI in the polymer backbone does not cause any chemical reaction between them, which can be substantiated by the presence of all characteristic peaks corresponding to pure P(VDF-HFP). The peaks about 761 cm^{-1} and 793 cm^{-1} correspond to the semi-crystalline α- phase of the P(VDF-HFP) polymer corroborating the XRD result of CSE-0. The addition of salt causes the transformation of α- phase to a mixture of β- & γ- phases of P(VDF-HFP), demonstrated by the shifting of intense peaks and disappearance of peaks observed around 761 and 793 cm^{-1} [75, 76]. The introduction of NASICON-type LZSP powder in the lithiated polymer matrix increases the intensity of the peak at 1668 cm^{-1}, indicating the enhancement in the dissociation of lithium salt. The peak observed at about 1100 cm^{-1} is prescribed to the P-O bond in the NASICON structure. Dissociation of LiTFSI salt is related to the intensity of the peak ~ 1136 cm^{-1} [72]. There was a slight increase in the intensity of the C=C stretching peak with the increase in the ceramic content, which indicates the partial dehydrofluorination and deprotonation of P(VDF-HFP) [77]. The ceramic LZSP filler acts as a Lewis acid enriching the dissociation of lithium salt, which causes intensity evolution in the FTIR spectra with increasing the fraction of ceramics in the polymer.

3.4. Thermal and Mechanical Properties

DSC experiment is carried out for CSE-0 and CSE-15 in the range of 60-245 ºC with a heating rate of 5 ºC / min to study the impact of ceramic filler on the crystallization of P(VDF-HFP) polymer [78]. Figure 3 presents the DSC thermograms of CSE-0 and CSE-15 in the heating cycle. 15% ceramic addition to the P(VDF-HFP)/LiTFSI matrix was found to decrease the crystallinity as confirmed by the reduction in the area of the melting peak. A decrease in the melting temperature from ~ 137 ºC for CSE-0 to ~ 127 ºC for CSE-15 is also observed. Attributing to the Gibbs-Thomson equation, the difference between the melting temperatures is inversely proportional to the crystal size, so smaller crystallites tend to melt at lower temperatures [79]. The increase in the volume of the amorphous region in the CSE-15 film helps in the facile polymer chain movement for lithium-ion conduction, but in the case of CSE-0 the polymer chain movement is hindered by the crystalline phases present in the polymer matrix providing sluggish lithium-ion conduction. The mechanical properties of CSE-0 and CSE-15 with a cross-sectional area of 0.50 mm^2 and a gauge length of 10 mm at 25 ºC were obtained using a UTM with a tensile loading speed of 5 mm/min. The stress-strain curves for CSE-0 and CSE-15 are given in Fig. S6. The tensile strength was increased from ~ 5.8 MPa for CSE-0 to 10.5 MPa for CSE-15. The presence of LZSP ceramic particles increased the tensile strength.

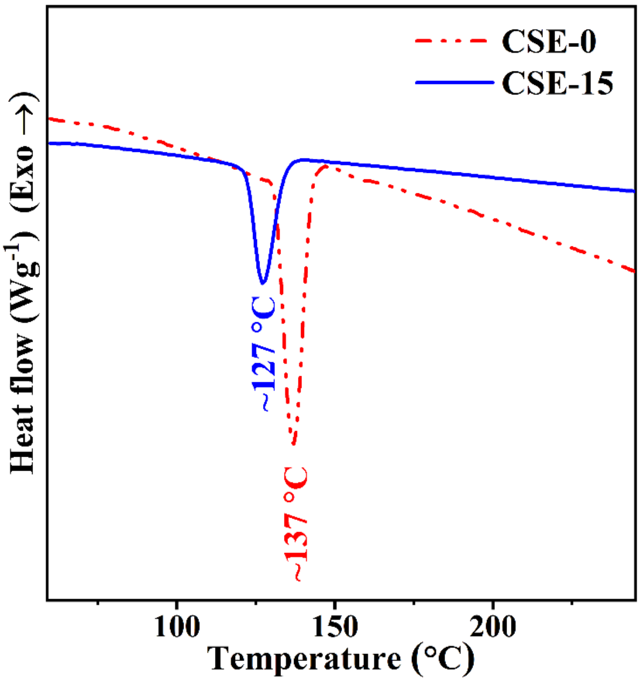

Fig. 3. *DSC thermograms of CSE-0 and CSE-15.*

3.5. Complex Impedance Analysis

Complex impedance analysis is a vital technique to measure the electrolytes' resistance by applying a suitable AC perturbation in a wide frequency range. The room temperature Nyquist plot for the sintered LZSP ceramic and composite electrolytes with different percentages of LZSP are shown in Fig. 4(a-j). For the LZSP pellet, the straight line seen in the low-frequency region is because of the ion's accumulation at the blocking electrodes surface (Fig. 4(a)). The grain and grain boundary contributions in the LZSP Nyquist plot appear as two semicircles in high and mid-frequency regimes due to the difference in their relaxation times (τ = RC). An equivalent circuit comprising two resistors and three constant phase elements (CPEs) shown in the inset of Fig. 4(a) was used to fit the experimental data. R1 and R2 represent the grain and grain boundary resistance, respectively. The element CPE3 accounts for the Li^+-blocking behavior of silver electrodes in the low-frequency regime. The fitted data is in good agreement with the experimental data. The bulk conductivity (σ_{RT}) was calculated to be 6.86 × 10^{-5} S/cm using (Eq. 1),

$$\sigma_{RT} = \frac{t}{R \times A} \tag{1}$$

(t = thickness of the pellet, R = resistance of the pellet, A = cross-sectional area of the pellet). Bulk ionic conductivities at different temperatures were calculated. The variation of the conductivity with the inverse of temperature for the sintered LZSP pellet is given in Fig. 5(a). Linear fitting of $\sigma(T)$ using the Arrhenius equation (Eq. 2) was carried out to find the activation energy (E_A),

$$\sigma(T) = \sigma_0 \, e^{\frac{-E_A}{k_B T}} \tag{2}$$

where σ_0= pre-exponential factor, E_A = activation Energy, k_B = Boltzmann's constant, and T = absolute temperature. The value of E_A was calculated to be ~ 0.47 ± 0.04 eV.

In the Nyquist plots of CSE-x (x = 0, 5, 10, 15, and 20), only a tail-like feature along with a partially formed semicircle can be observed. The tail is ascribed to stainless steel electrodes' ion-blocking nature, and the semi-circular arc is due to the bulk response of the sample in the high-frequency region. With the increase in the concentration of ceramic filler ($x \leq 15\%$), an increase in the conductivity can be inferred from the concomitant shifting of the low-frequency intercept of the semi-circular arc on the real axis in the Nyquist plot. Room temperature (RT) conductivity was estimated by modelling the complex impedance data using the equivalent circuit consisting of a series connection of a CPE2 with another parallel circuit of another CPE1 and a resistor R1 (shown as Fig. 4(b) inset). The RT conductivity values of different composite samples were calculated using the fitted values of R1 and sample dimensions (see Table 2). A continuous increase in ionic conductivity was observed with increasing ceramic concentration up to 15%, while a decrease in ionic conductivity for CSE-20 was noticed.

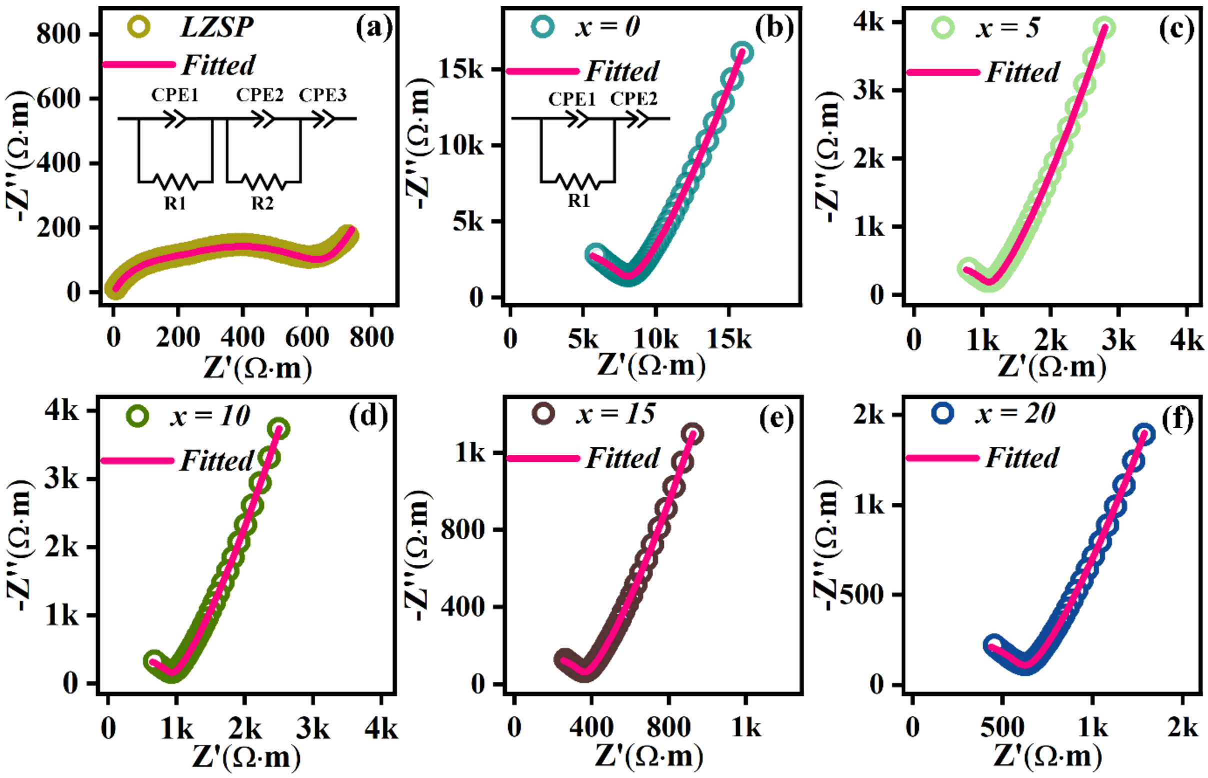

Fig. 4. *Room temperature Nyquist plots of LZSP ceramics and CSE-x (x = 0, 5, 10, 15, and 20). Fig. 4(a) & 4(b) insets display the equivalent circuits used for fitting the impedance data of LZSP sample & CSE-x (x = 0, 5, 10, 15, and 20).*

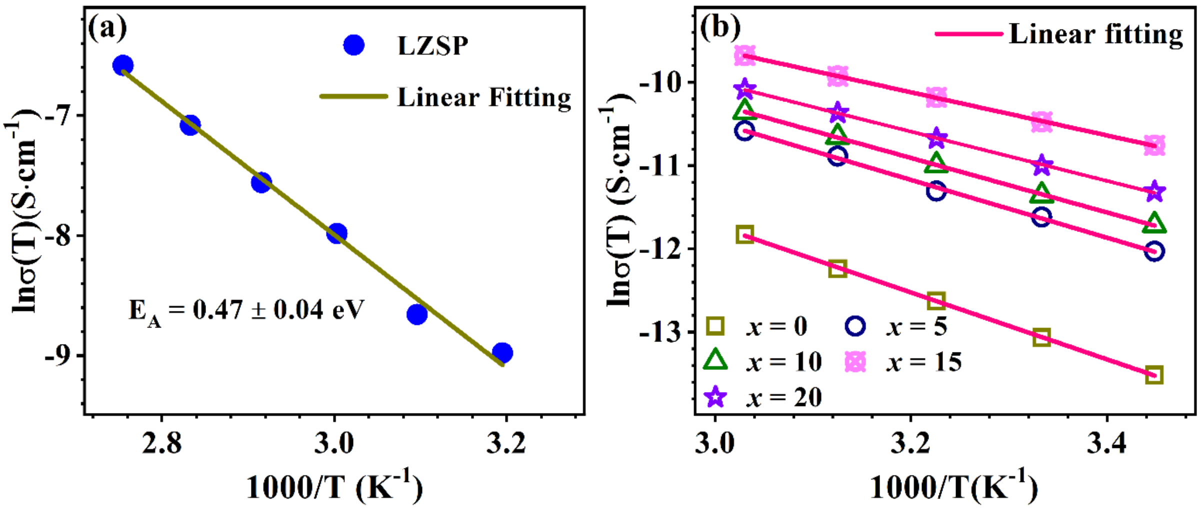

Fig. 5. *Linear fitting using Arrhenius equation for (a) LZSP pellet and (b) CSE-x (x = 0, 5, 10, 15, and 20).*

A maximum room temperature conductivity of 2.87×10^{-5} S/cm was obtained for CSE-15. CSE-0 has the lowest conductivity of 2.1×10^{-6} S/cm at room temperature due to sluggish ionic movements in the crystalline phase present in the lithiated polymer matrix. The addition of ceramic powders in polymers is known to decrease the semi-crystallinity of polymer matrix as reported in the literature [80, 81]. It is believed that lithium-ion conduction is more facile in the amorphous phase than in the crystalline phase [82].

At the ceramic percentage of 15%, conductivity attained the local maximum leveraged by additional conduction pathways for the Li^+ movement through the LZSP particles and a decrease in the crystalline nature of the polymer-salt matrix, as discussed in the DSC analysis. Further temperature-dependent conductivity measurements were carried out to determine the activation energy *via* linear fitting of the Arrhenius equation (Eq. 2) and the fitted results are presented in Fig. 5(b). The activation energy calculated for different samples is given in Table 2. The sample (CSE-15) with maximum conductivity also exhibited minimum activation energy of 0.220 ± 0.007 eV. The Li^+ conduction becomes facile through the space charge region formed at the interface of the polymer matrix and ceramic particles due to Lewis acid-base interaction [83]. However, the agglomeration effect came into the picture owing to an increase in ceramic concentration hindering the lithium-ion conduction through the polymer matrix. Thus, the CSE-20 sample showed lesser conductivity and higher activation energy than the CSE-15 sample.

3.6. Electrochemical performance

Cyclic voltammetry test was performed on the symmetric cell prepared with Li-metal on either side with CSE-15 in the voltage range –1.7 V to +1.7 V at a scan rate of 0.1 mV/s to confirm the lithium-ion conduction through the solid electrolyte, and the results are illustrated in Fig. 6(a). The anodic and cathodic peaks are found to be –0.35 V and +0.35 V, respectively, which confirms the facile lithium-ion conduction through the CSE-15. The difference between oxidation and reduction peak voltages is 0.7 V indicating the reversible uniform plating and stripping of lithium on both electrodes' surfaces. With the increase in the number of cycles, a decrease in response current for lithium plating and stripping was observed due to the increase in resistance ascribed to the interphase layer formation driven by interfacial reaction between the composite solid electrolyte and the highly reactive lithium metal, which is supposed to stabilize the anode-electrolyte interfacial resistance during continuous cycling of charging and discharging.

Symmetric cell CV measurements were followed up with cyclic voltammetry tests on the asymmetric cell (Li|CSE-15|SS) fabricated by sandwiching the CSE-15 membrane between asymmetric electrodes Li metal and stainless steel. Fig. 6(b) displays the outcome of the CV carried out in the voltage range of –0.6 V to +3.5 V at a scan rate of 0.1 mV/s. The facile lithium-ion conduction was again confirmed by the anodic and cathodic peaks found at –0.6 V and +0.3 V due to the plating and stripping of Li on the stainless steel, respectively. When the voltage scanned below zero potential, a linear increase in current indicates the lithium depletion from the lithium metal electrode and lithium deposition on the stainless steel. During the back scan from pre-set –0.6 V to 0 V, the CV curve almost retraces the original path. After 0 V, a nonlinear increase in positive current was observed due to lithium dissolution from the surface of stainless steel, and the current reaches a maximum at +0.3 V, then decreases to a small current value indicating the limited numbers of lithium atoms available for stripping out. The redox currents remain nearly constant for the concordant cycles signifying the high reversibility of lithium deposition and dissolution on the stainless steel through the CSE-15. Again, no redox peak after 0.3 V signifies the expected electrochemical stability of CSE-15. Cyclic voltammetry performed on symmetric cells (with two non-blocking electrodes), and asymmetric cells (with one non-blocking electrode and another blocking electrode) corroborate the reversible lithium-ion conduction through the CSE-15. The Bruce-Vincent method is used to determine the lithium-ion transference number [84]. The equation used to calculate the cationic transference number is given by (Eq. 3),

$$t_{Li^+} = \frac{I_{ss}(\Delta \mathrm{V} - I_o R_o)}{I_o(\Delta \mathrm{V} - I_{ss} R_{ss})} \tag{3}$$

I_o & R_o are the initial current & initial interface resistance, respectively, prior to DC field polarization and I_{ss} & R_{ss} are the steady state current & interfacial resistance after DC field polarization The interfacial resistances were calculated using the appropriate equivalent circuit shown in Fig. 7(a) inset. The result of the test performed at room temperature (25 ºC) for CSE-15 is shown in tig. 7(a) where ΔV = 50 mV. The initial current of 18 µA (at time t = 0) decayed exponentially to a steady state current value of ~ 10 µA (at t = 4 h). The Nyquist plots (frequency range of 1 Hz to 1 MHz) of the tested cell before and after polarisation are shown in the figure inset.

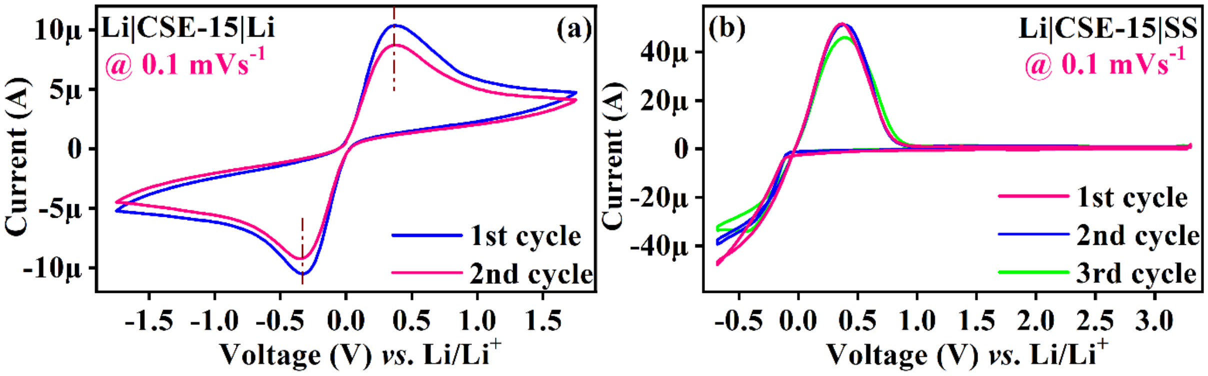

Fig. 6. *Cyclic voltammetry on (a) symmetric Li|CSE-15|Li cell and (b) asymmetric Li|CSE-15|SS cell.*

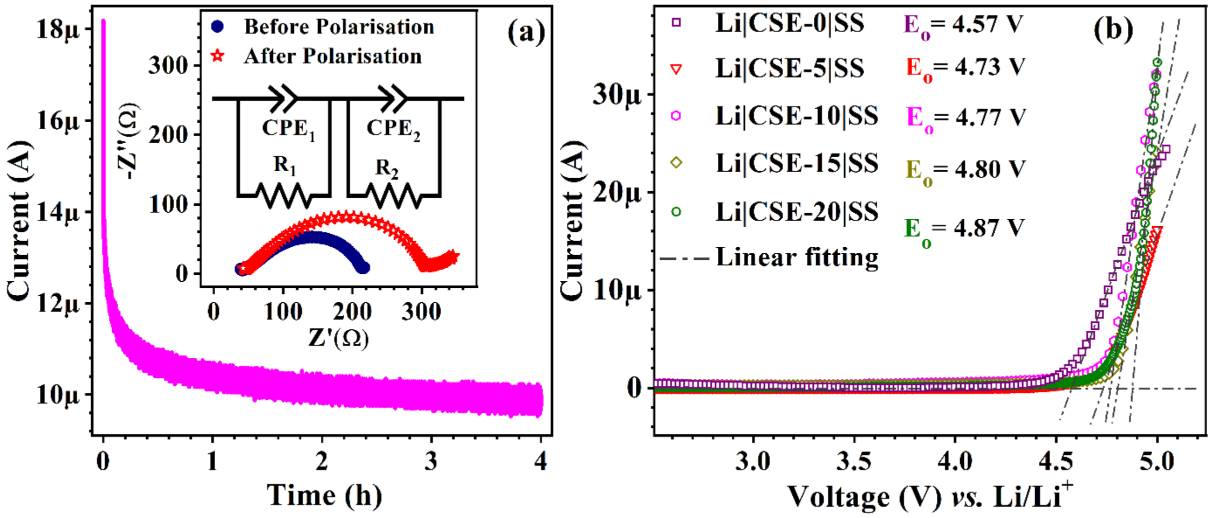

Fig. 7. *(a)Current variation with time upon applying 0.05 V on symmetric Li|CSE-15|Li cell. The Inset figure shows the Nyquist plots before and after dc polarisation and the equivalent circuit fitted for the calculation of interfacial resistance. (b) Linear sweep voltammetry of CSE-0, CSE-5, CSE-10, CSE-15, and CSE-20.*

The high-frequency intercept provides the bulk resistance of the composite electrolyte, and charge transfer resistance at the electrode-electrolyte interface is given by the low-frequency intercept. The difference between the charge transfer resistance and bulk resistance provides the interfacial resistance. No significant change in bulk resistance was observed, whereas the interfacial resistance increased from 175 Ω to 250 Ω. Table 3 presents the lithium-ion transference number calculated for all the samples using Eq. 3. The electrolyte with 15% ceramic content showed the highest transference number of ~ 0.55, following the same trend of ionic conductivity. NASICON ceramic particles are known to have a very high Li-ion transference number (close to 1, in many cases). NASICON fillers also hinder the movement of (TFSI)$^-$ and poly-ions [comprising of Li$^+$ and (TFSI)$^-$] due to their larger sizes compared to the Li$^+$. Accordingly, the CSE-15 composite is expected to exhibit a higher Li-ion transference number as compared to CSE-0 (polymer-salt sample). Moreover, the LZSP particles could act as the Lewis acid sites which could cause the complexation between (TFSI)$^-$ and LZSP particles. Thus, the addition of ceramics enhances the lithium-ion transference number. CSE-20 electrolyte showed a decline in lithium-ion transference number as compared to CSE-15.

This decrement could be associated with the less surface area exposed for Lewis acid-base interactions due to the agglomeration of LZSP particles, as shown in SEM images provided in Supplementary Materials (Figs. S4 & S5).

Linear Sweep voltammetry (LSV) is a widely accepted technique to determine an electrolyte's electrochemical stability window (ESW). The onset of the current in the anodic high-voltage range is assumed to have resulted from the decomposition of electrolytes, and this onset voltage is taken as the upper limit of the electrolyte stability range. LSV has been performed on the asymmetric cells Li|CSE|SS in the voltage window ranging from 2.5 V to 5 V at a scan rate of 0.1 mV/s. A steady small current flow through the CSEs was recorded at low voltages, but the onset of current was observed beyond a critical voltage, which is attributed to the decomposition of electrolytes. The intersection point of linear fittings in the low current region and the high current region provides the upper cut-off voltage value. The critical voltage of ~ 4.80 V is determined for the CSE-15 sample, which ensures the application of high-voltage cathode-like spinel type $LiMn_2O_4$, layered oxides, etc. The LSV carried out for all compositions is shown in Fig. 7(b).

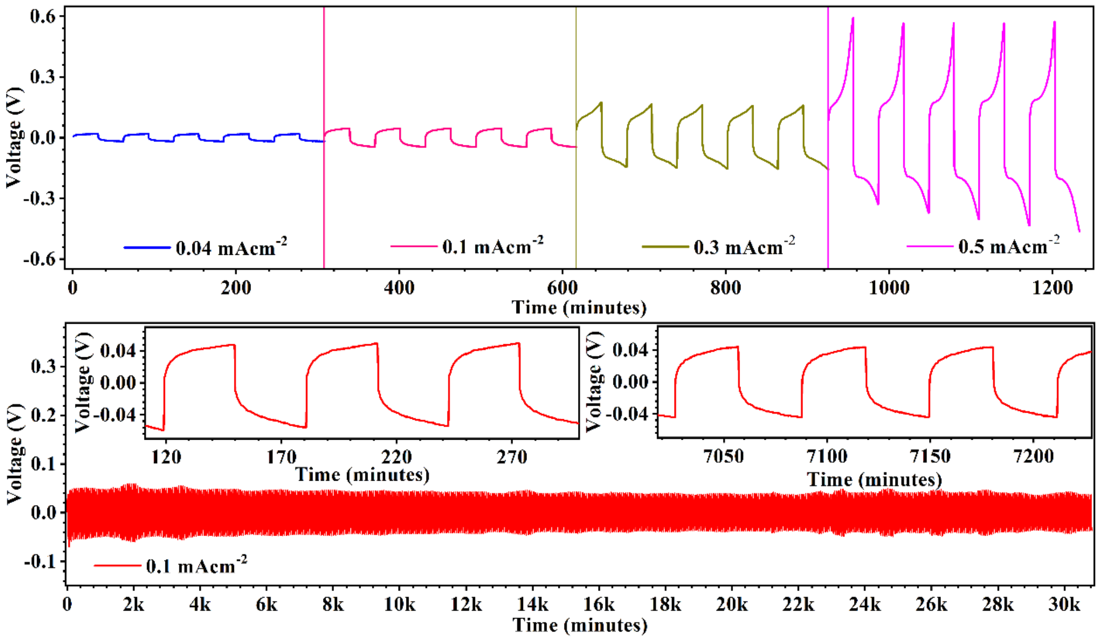

Fig. 8. *Galvanostatic charge- discharge profile of symmetric Li|CSE-15|Li cell.*

Galvanostatic charging and discharging (GCD) of symmetric cells with lithium metal as electrodes provide the context of the durability and feasibility of application in batteries. Voltage responses of symmetric Li|CSE-15|Li at room temperature were recorded for more than 500 hours with different current densities at room temperature, one cycle being 30 minutes of charge and 30 minutes of discharge, and the GCD profile was given in Fig. 8. With current densities from 0.04 mA/cm^2 to 0.5 mA/cm^2 and more than 180 hours of continuous cycling, no sign of short-circuit was observed. For 0.04 mA/cm^2, a voltage plateau at ~ 18 mV was seen. With an increment in the value of current density from 0.04 mA/cm^2 to 0.1 mA/cm^2, the plateau voltage level shifts to ~ 50 mV. Further, at 0.3 mA/cm^2, the voltage level increased steadily, and the plateau maintained symmetry in the initial charging and discharging cycles. But the symmetrical voltage response disappeared at a current density of 0.5 mA/cm^2 without any voltage plateau during charging and discharging. The obtained symmetric charging and discharging profiles for all the current densities below the critical current density of ~ 0.5 mA/cm^2 connote the good contact of CSE-15 film on both sides with the lithium metal. No change in the over-potential for 0.1 mA/cm^2 was observed while decreasing the current density from 0.5 mA/cm^2 to 0.1 mA/cm^2, indicating high reversibility to sustain different C-rates charging and discharging in practical battery applications for a longer duration. To demonstrate the durability and feasibility of the composite polymer electrolyte (CSE-15) over the polymer electrolyte (CSE-0), a GCD profile of symmetric Li|CSE-0|Li cell is provided in Fig. S7 (Supplementary Materials). At the current density of 0.04 mA/cm^2, the polarisation potential in Li|CSE-0|Li was ~ 190 mV which is nearly 4.5 times as compared to that of Li|CSE-15|Li. On increasing the current density to 0.1 mA/cm^2, the voltage profile becomes more asymmetric and non-uniform during the constant current pulse. Further, an unexpected decrease in overpotential with cycling was observed, followed by continuous voltage fluctuation in the form of "peaks" and "arcing" in the GCD curve of Li|CSE-0|Li. A similar phenomenon has been reported in several articles, and the accumulation of dead lithium and the resulting spatial heterogeneity in reaction kinetics on the lithium anode surface is believed to be responsible for such voltage profiles [85, 86]. The photographs of lithium metal electrodes, CSE-0, and CSE-15 solid electrolytes harvested from the de-crimped (in a glove box with O_2 & H_2O < 0.1 ppm) symmetric cells after 100 cycles, are shown in Fig. S8 in Supplementary Materials. The color of the CSE-0 electrolyte changed to brown upon cycling. This color change suggests a reaction between the lithium metal and electrolyte, forming a distinct interface. Formation of such interfacial layers between the electrolyte and Li metal electrode is known to be a slow process that leads to an increase in interfacial impedance with time up to many days [41].

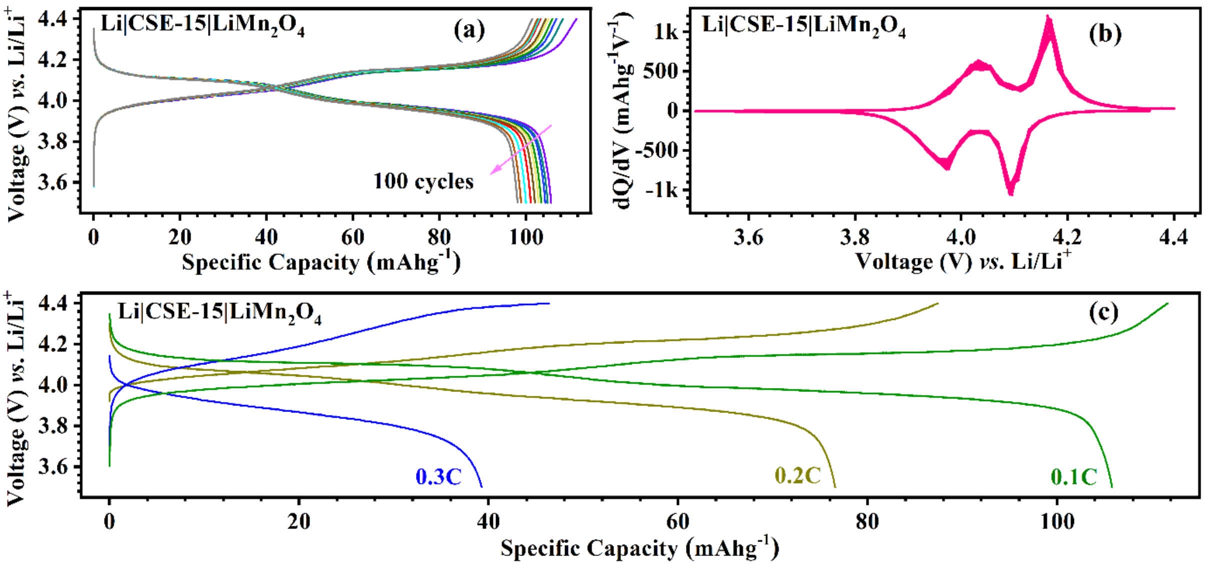

Fig. 9. *(a) Galvanostatic charge-discharge profile of full Li|CSE-15|LMO cell at 0.1 C-rate, (b) differential capacity plot of full Li|CSE-15|LMO at the constant current density of 0.1 mA/cm^2, and (c) galvanostatic charge-discharge profile of full Li|CSE-15|LMO at different C-rates.*

The galvanostatic charging and discharging of fabricated Li|CSE-15|LMO cell was carried out at room temperature (25 ºC) with a lower cut-off voltage of 3.5 V and an upper cut-off voltage of 4.4 V to avoid the detrimental structure transformation from *Spinel* type to *Layered* type [87]. The results shown in Fig. 9(a) depicted an initial discharge capacity of ~105 mAh/g (calculated using the loading of LMO) at 0.1C-rate (the practical, specific capacity of LMO ~ 110 mAh/g). Low columbic efficiency of ~ 94.7% in the first few cycles is attributed to the side reactions and forming stable SEI formation, whereas, further cycling at 0.1C, the columbic efficiency improved to nearly 99%. After 100 cycles, the capacity is reduced to 98 mAh/g with 93% capacity retention. This reduction could be due to modification in LMO structure, continuous inevitable, irreversible side reactions, and an increase in electrolyte-electrode interfacial resistance. On increasing the current density, capacity faded to 77 mAh/g and 40 mAh/g at 0.2C and 0.3C, respectively, as shown in Fig. 9(c). This drastic reduction in capacity could be due to increased overpotential developed between the electrode and electrolyte interface. The differential capacity (dQ/dV) plot of Li|CSE-15|LMO showed the intercalation and deintercalation potentials of the cathode material at a constant current rate of 0.1 mA/cm^2 (Fig. 9(b)). The peaks around 4.03 and 4.16 V correspond to the deintercalation of Li from the spinel LMO, and the intercalation potentials of Li into the spinel structure are at ~ 3.96 and 4.09 V.

4. Conclusions

The NASICON-type LZSP powders were successfully incorporated in the P(VDF-HFP) polymer matrix lithiated by LiTFSI salt to fabricate the thin composite solid electrolytes. The effect of various concentrations of ceramic filler on the structural properties, electrical properties, and electrochemical properties was studied. The uniform distribution of LZSP particles in the composite electrolyte was observed from the FESEM images and EDS data. Among all samples, the maximum ionic conductivity, the minimum activation energy, and the maximum lithium-ion transference number were determined to be ~ 2.87×10^{-5} S/cm, ~ 0.22 eV, and ~ 0.55, respectively, for samples with 15 wt.% of LZSP filler. This improvement was attributed to the efficient lithium-ion conduction paths provided by the LZSP particles acting as an active filler in the polymer matrix. The CV tests on symmetric and asymmetric cells showed the compatibility of composite electrolytes with lithium metal. For CSE-15, the electrochemical stability window (ESW) was ~ 4.80 V. The (Li|CSE-15|LMO) cell delivered a discharge capacity of ~ 105 mAh/g (rated specific capacity of LMO ~ 110 mAh/g) with a 93% retention after 100 cycles at a 0.1C rate. The overall improved properties suggest that the CSE-15 composite electrolyte is a good candidate for rechargeable all-solid-state lithium batteries.

Conflicts of interest:

There are no conflicts to declare.

Acknowledgments:

The authors thank the Science and Engineering Research Board (SERB) for the Core Research Grant (Grant no. CRG/2021/005548). Department of Science and Technology (DST), Government of India is also gratefully acknowledged for funding (Grant no. DST/TMD/IC-MAP/2K20/01). The authors are grateful to Prof. I.A. Palani, Mechatronics and Instrumentation Lab, Department of Mechanical Engineering, Indian Institute of Technology Indore, India for providing a DSC facility.

References

[1] M. Winter, B. Barnett, K. Xu, Before Li Ion Batteries, Chem. Rev., 118 (2018) 11433.

[2] J.B. Goodenough, K.-S. Park, The Li-Ion Rechargeable Battery: A Perspective, J. Am. Chem. Soc., 135 (2013) 1167.

[3] B. Diouf, R. Pode, Potential of lithium-ion batteries in renewable energy, Renew. Energ., 76 (2015) 375.

[4] X.-B. Cheng, R. Zhang, C.-Z. Zhao, Q. Zhang, Toward Safe Lithium Metal Anode in Rechargeable Batteries: A Review, Chem. Rev., 117 (2017) 10403.

[5] C.P. Grey, D.S. Hall, Prospects for lithium-ion batteries and beyond—a 2030 vision, Nat. Commun., 11 (2020) 6279.

[6] S. Megahed, W. Ebner, Lithium-ion battery for electronic applications, J. Power Sources, 54 (1995) 155.

[7] E.C. Evarts, Lithium batteries: To the limits of lithium, Nature, 526 (2015) S93.

[8] A. Kwade, W. Haselrieder, R. Leithoff, A. Modlinger, F. Dietrich, K. Droeder, Current status and challenges for automotive battery production technologies, Nat. Energy, 3 (2018) 290.

[9] W. Li, E.M. Erickson, A. Manthiram, High-nickel layered oxide cathodes for lithium-based automotive batteries, Nat. Energy, 5 (2020) 26.

[10] W. Li, B. Song, A. Manthiram, High-voltage positive electrode materials for lithium-ion batteries, Chem. Soc. Rev., 46 (2017) 3006.

[11] N. Nitta, F. Wu, J.T. Lee, G. Yushin, Li-ion battery materials: present and future, Mater. Today, 18 (2015) 252.

[12] R. Schmuch, R. Wagner, G. Hörpel, T. Placke, M. Winter, Performance and cost of materials for lithium-based rechargeable automotive batteries, Nat. Energy, 3 (2018) 267.

[13] J.C. Bachman, S. Muy, A. Grimaud, H.-H. Chang, N. Pour, S.F. Lux, O. Paschos, F. Maglia, S. Lupart, P. Lamp, L. Giordano, Y. Shao-Horn, Inorganic Solid-State Electrolytes for Lithium Batteries: Mechanisms and Properties Governing Ion Conduction, Chem. Rev., 116 (2016) 140-162.

[14] S.A. Ahmed, T. Pareek, S. Dwivedi, M. Badole, S. Kumar, $LiSn_2(PO_4)_3$-based polymer-in-ceramic composite electrolyte with high ionic conductivity for all-solid-state lithium batteries, J. Solid State Electrochem., 24 (2020) 2407-2417.

[15] X. Zhao, P. Xiang, J. Wu, Z. Liu, L. Shen, G. Liu, Z. Tian, L. Chen, X. Yao, Toluene Tolerated $Li_{9.88}GeP_{1.96}Sb_{0.04}S_{11.88}Cl_{0.12}$ Solid Electrolyte toward Ultrathin Membranes for All-Solid-State Lithium Batteries, Nano Lett., 23 (2023) 227-234.

[16] T. Pareek, S. Dwivedi, B. Singh, D. Kumar, P. Kumar, S. Kumar, $LiSnZr(PO_4)_3$: NASICON-type solid electrolyte with excellent room temperature Li^+ conductivity, J. Alloys Compd., 777 (2019) 602-611.

[17] Q. Guo, F. Xu, L. Shen, S. Deng, Z. Wang, M. Li, X. Yao, 20 μm-Thick $Li_{6.4}La_3Zr_{1.4}Ta_{0.6}O_{12}$-Based Flexible Solid Electrolytes for All-Solid-State Lithium Batteries, Energy Mater. Adv., 2022 (2022) 9753506.

[18] Q. Guo, F. Xu, L. Shen, Z. Wang, J. Wang, H. He, X. Yao, Poly(ethylene glycol) brush on $Li_{6.4}La_3Zr_{1.4}Ta_{0.6}O_{12}$ towards intimate interfacial compatibility in composite polymer electrolyte for flexible all-solid-state lithium metal batteries, J. Power Sources, 498 (2021) 229934.

[19] X. Huang, Z. Song, T. Xiu, M.E. Badding, Z. Wen, Sintering, micro-structure and Li+ conductivity of $Li_{7-x}La_3Zr_{2-x}Nb_xO_{12}$/MgO ($x = 0.2–0.7$) Li-Garnet composite ceramics, Ceram. Int., 45 (2019) 56-63.

[20] V. Ramar, S. Kumar, S.R. Sivakkumar, P. Balaya, NASICON-type La^{3+}substituted $LiZr_2(PO_4)_3$ with improved ionic conductivity as solid electrolyte, Electrochim. Acta, 271 (2018) 120-126.

[21] T. Pareek, B. Singh, S. Dwivedi, A.K. Yadav, Anita, S. Sen, P. Kumar, S. Kumar, Ionic conduction and vibrational characteristics of Al^{3+} modified monoclinic $LiZr_2(PO_4)_3$, Electrochim. Acta, 263 (2018) 533-543.

[22] S. Kumar, P. Balaya, Improved ionic conductivity in NASICON-type Sr^{2+} doped $LiZr_2(PO_4)_3$, Solid State Ion., 296 (2016) 1-6.

[23] A. Loutati, P. Odenwald, B. Aktekin, J. Sann, O. Guillon, F. Tietz, D. Fattakhova-Rohlfing, Survey of Zirconium-Containing NaSICON-type Solid-State Li+ Ion Conductors with the Aim of Increasing Reduction Stability by Partial Cation Substitution, Batter. Supercaps, 5 (2022) e202200327.

[24] M.A. Subramanian, R. Subramanian, A. Clearfield, Lithium ion conductors in the system $AB(IV)_2(PO_4)_3$ (B = Ti, Zr and Hf), Solid State Ion., 18-19 (1986) 562-569.

[25] H. Aono, E. Sugimoto, Y. Sadaoka, N. Imanaka, G.-y. Adachi, Ionic conductivity and sinterability of lithium titanium phosphate system, Solid State Ion., 40-41 (1990) 38-42.

[26] X. Xu, Z. Wen, X. Wu, X. Yang, Z. Gu, Lithium Ion-Conducting Glass–Ceramics of $Li_{1.5}Al_{0.5}Ge_{1.5}(PO_4)_3–xLi_2O$ (x=0.0–0.20) with Good Electrical and Electrochemical Properties, J. Am. Ceram. Soc., 90 (2007) 2802-2806.

[27] H. Xie, J.B. Goodenough, Y. Li, $Li_{1.2}Zr_{1.9}Ca_{0.1}(PO_4)_3$, a room-temperature Li-ion solid electrolyte, J. Power Sources, 196 (2011) 7760-7762.

[28] Y. Li, M. Liu, K. Liu, C.-A. Wang, High Li^+ conduction in NASICON-type $Li_{1+x}Y_xZr_{2-x}(PO_4)_3$ at room temperature, J. Power Sources, 240 (2013) 50-53.

[29] Q. Zhou, B. Xu, P.-H. Chien, Y. Li, B. Huang, N. Wu, H. Xu, N.S. Grundish, Y.-Y. Hu, J.B. Goodenough, NASICON $Li_{1.2}Mg_{0.1}Zr_{1.9}(PO_4)_3$ Solid Electrolyte for an All-Solid-State Li-Metal Battery, Small Methods, 4 (2020) 2000764.

[30] G.G. Amatucci, A. Safari, F.K. Shokoohi, B.J. Wilkens, Lithium scandium phosphate-based electrolytes for solid state lithium rechargeable microbatteries, Solid State Ion., 60 (1993) 357-365.

[31] X. Yu, A. Manthiram, A review of composite polymer-ceramic electrolytes for lithium batteries, Energy Storage Mater., 34 (2021) 282-300.

[32] D.E. Fenton, J.M. Parker, P.V. Wright, Complexes of alkali metal ions with poly(ethylene oxide), Polymer, 14 (1973) 589.

[33] Z. Wang, B. Huang, H. Huang, L. Chen, R. Xue, F. Wang, Investigation of the position of Li+ ions in a polyacrylonitrile-based electrolyte by Raman and infrared spectroscopy, Electrochim. Acta, 41 (1996) 1443-1446.

[34] E. Cazzanelli, G. Mariotto, G.B. Appetecchi, F. Croce, B. Scrosati, Study of ion-molecule interaction in poly(methylmethacrylate) based gel electrolytes by raman spectroscopy, Electrochim. Acta, 40 (1995) 2379-2382.

[35] Y. Tominaga, K. Yamazaki, V. Nanthana, Effect of Anions on Lithium Ion Conduction in Poly(ethylene carbonate)-based Polymer Electrolytes, J. Electrochem. Soc., 162 (2015) A3133.

[36] A.M. Sukeshini, A. Nishimoto, M. Watanabe, Transport and electrochemical characterization of plasticized poly(vinyl chloride) solid electrolytes, Solid State Ion., 86-88 (1996) 385-393.

[37] D. Saikia, H.-Y. Wu, Y.-C. Pan, C.-P. Lin, K.-P. Huang, K.-N. Chen, G.T.K. Fey, H.-M. Kao, Highly conductive and electrochemically stable plasticized blend polymer electrolytes

based on PVdF-HFP and triblock copolymer PPG-PEG-PPG diamine for Li-ion batteries, J. Power Sources, 196 (2011) 2826-2834.

[38] C. Capiglia, Y. Saito, H. Kataoka, T. Kodama, E. Quartarone, P. Mustarelli, Structure and transport properties of polymer gel electrolytes based on PVdF-HFP and $LiN(C_2F_5SO_2)_2$, Solid State Ion., 131 (2000) 291-299.

[39] M.S. Grewal, M. Tanaka, H. Kawakami, Free-standing polydimethylsiloxane-based cross-linked network solid polymer electrolytes for future lithium ion battery applications, Electrochim. Acta, 307 (2019) 148-156.

[40] Z. Wang, L. Shen, S. Deng, P. Cui, X. Yao, 10 μm-Thick High-Strength Solid Polymer Electrolytes with Excellent Interface Compatibility for Flexible All-Solid-State Lithium-Metal Batteries, Adv. Mater., 33 (2021) 2100353.

[41] T. Pareek, S. Dwivedi, S.A. Ahmad, M. Badole, S. Kumar, Effect of NASICON-type $LiSnZr(PO_4)_3$ ceramic filler on the ionic conductivity and electrochemical behavior of PVDF based composite electrolyte, J. Alloys Compd., 824 (2020) 153991.

[42] Z. Wei, S. Chen, J. Wang, Z. Wang, Z. Zhang, X. Yao, Y. Deng, X. Xu, A large-size, bipolar-stacked and high-safety solid-state lithium battery with integrated electrolyte and cathode, J. Power Sources, 394 (2018) 57-66.

[43] S. Choudhary, R.J. Sengwa, Effects of different inorganic nanoparticles on the structural, dielectric and ion transportation properties of polymers blend based nanocomposite solid polymer electrolytes, Electrochim. Acta, 247 (2017) 924-941.

[44] S. Borah, A.K. Guha, L. Saikia, M. Deka, Nanofiber induced enhancement of electrical and electrochemical properties in polymer gel electrolytes for application in energy storage devices, J. Alloys Compd., 886 (2021) 161173.

[45] B. Luo, W. Wang, Q. Wang, W. Ji, G. Yu, Z. Liu, Z. Zhao, X. Wang, S. Wang, J. Zhang, Facilitating ionic conductivity and interfacial stability via oxygen vacancies-enriched TiO_2 microrods for composite polymer electrolytes, Chem. Eng. J., 460 (2023) 141329.

[46] K. Khan, B. Fu, H. Xin, B.A. Beshiwork, M.B. Hanif, J. Wu, Z. Fang, J. Yang, T. Li, C. Chen, M. Motola, Z. Xu, M. Wu, Composite polymer electrolyte incorporating WO_3 nanofillers with enhanced performance for dendrite-free solid-state lithium battery, Ceram. Int., 49 (2023) 4473-4481.

[47] J. Wei, X. Zheng, W. Lin, Y. Si, K. Ji, C. Wang, M. Chen, Retarding Li dendrites growth via introducing porous g-C_3N_4 into polymer electrolytes for solid-state lithium metal batteries, J. Alloys Compd., 909 (2022) 164825.

[48] T. Yang, J. Zheng, Q. Cheng, Y.-Y. Hu, C.K. Chan, Composite Polymer Electrolytes with $Li_7La_3Zr_2O_{12}$ Garnet-Type Nanowires as Ceramic Fillers: Mechanism of Conductivity Enhancement and Role of Doping and Morphology, ACS Appl. Mater. Interfaces, 9 (2017) 21773-21780.

[49] P. Sivaraj, K.P. Abhilash, B. Nalini, P. Perumal, P.C. Selvin, Free-standing, high Li-ion conducting hybrid PAN/PVdF/$LiClO_4$/$Li_{0.5}La_{0.5}TiO_3$ nanocomposite solid polymer electrolytes for all-solid-state batteries, J. Solid State Electrochem., 25 (2021) 905-917.

[50] B.-J. Sung, P.N. Didwal, R. Verma, A.-G. Nguyen, D.R. Chang, C.-J. Park, Composite solid electrolyte comprising poly(propylene carbonate) and $Li_{1.5}Al_{0.5}Ge_{1.5}(PO_4)_3$ for long-life all-solid-state Li-ion batteries, Electrochim. Acta, 392 (2021) 139007.

[51] S. Li, J. Lu, Z. Geng, Y. Chen, X. Yu, M. He, H. Li, Solid Polymer Electrolyte Reinforced with a $Li_{1.3}Al_{0.3}Ti_{1.7}(PO_4)_3$-Coated Separator for All-Solid-State Lithium Batteries, ACS Appl. Mater. Interfaces, 14 (2022) 1195-1202.

[52] T. Wang, X. Liu, L. Xie, Y. He, H. Ji, L. Wang, X. Niu, J. Gao, 3D nanofiber framework based on polyacrylonitrile and siloxane-modified $Li_{6.4}La_3Zr_{1.4}Ta_{0.6}O_{12}$ reinforced poly (ethylene oxide)-based composite solid electrolyte for lithium batteries, J. Alloys Compd., 945 (2023) 168877.

[53] R.J. Pei, Y.F. Li, T. Song, N. Chen, R. Yang, A solid composite electrolyte of 3D framework $Li_{6.25}La_3Sn_{1.25}Bi_{0.75}O_{12}$ for rechargeable solid-state batteries, J. Alloys Compd., 933 (2023) 167639.

[54] N. Lv, Q. Zhang, Y. Xu, H. Li, Z. Wei, Z. Tao, Y. Wang, H. Tang, PEO-based composite solid electrolyte for lithium battery with enhanced interface structure, J. Alloys Compd., 938 (2023) 168675.

[55] X. Hao, K. Chen, Y. Tang, X. Zhong, K. Cai, 2-Dimensional g-C_3N_4 nanosheets modified LATP-based "Polymer-in-Ceramic" electrolyte for solid-state lithium batteries, J. Alloys Compd., 942 (2023) 169064.

[56] D. Han, Z. Zhao, W. Wang, H. Wang, J. Shi, L. Zheng, Vanadium doped ceramic matrix $Li_{6.7}La_3Zr_{1.7}V_{0.3}O_{12}$ enabled PEO-based solid composite electrolyte with high lithium ion transference number and cycling stability, Ceram. Int., 49 (2023) 7935-7945.

[57] Z.H. Huang, M.X. Jing, P.Q. Wang, W.W. Shao, Z.P. Zhang, G. Zhang, X.Q. Shen, A high ionic conductive PDOL/LAGP composite solid electrolyte film for Interfacial Stable solid-state lithium batteries, Ceram. Int., 49 (2023) 5510-5517.

[58] X. Lu, J. Hai, F. Zhang, X. Li, J. Li, Preparation and infiltration of NASICON-type solid electrolytes with microporous channels, Ceram. Int., 48 (2022) 2203-2211.

[59] Z. Zhang, Y. Huang, H. Gao, J. Huang, C. Li, P. Liu, An all-solid-state lithium battery using the $Li_7La_3Zr_2O_{12}$ and $Li_{6.7}La_3Zr_{1.7}Ta_{0.3}O_{12}$ ceramic enhanced polyethylene oxide electrolytes with superior electrochemical performance, Ceram. Int., 46 (2020) 11397-11405.

[60] H. Fan, F. Wei, J. Luo, S. Wu, X. Jian, W. Lan, K. Zhang, R. Zeng, H. Chen, R. Zhao, Interfacial engineering facilitating robust $Li_{6.35}Ga_{0.15}La_3Zr_{1.8}Nb_{0.2}O_{12}$ for all-solid-state lithium batteries, Sustain. Energy Fuels, 5 (2021) 2077-2084.

[61] G. Yu, Y. Wang, K. Li, D. Chen, L. Qin, H. Xu, J. Chen, W. Zhang, P. Zhang, Z. Sun, Solution-processable $Li_{10}GeP_2S_{12}$ solid electrolyte for a composite electrode in all-solid-state lithium batteries, Sustain. Energy Fuels, 5 (2021) 1211-1221.

[62] J.-c. Seol, R. Balasubramaniam, V. Aravindan, R. Thangavel, Y.-S. Lee, Ameliorating the electrode/electrolyte interface compatibility in Li-ion solid-state batteries with plasticizer, J. Alloys Compd., 927 (2022) 167077.

[63] A. Coelho, TOPAS and TOPAS-Academic: an optimization program integrating computer algebra and crystallographic objects written in C++, J. Appl. Crystallogr., 51 (2018) 210-218.

[64] B. Akkinepally, I.N. Reddy, V. Manjunath, M.V. Reddy, Y.K. Mishra, T.J. Ko, K. Zaghib, J. Shim, Temperature effect and kinetics, $LiZr_2(PO_4)_3$ and $Li_{1.2}Al_{0.2}Zr_{1.8}(PO_4)_3$ and electrochemical properties for rechargeable ion batteries, Int. J. Energy Res., 46 (2022) 14116-14132.

[65] K. Momma, F. Izumi, VESTA: a three-dimensional visualization system for electronic and structural analysis, J. Appl. Crystallogr., 41 (2008) 653-658.

[66] I.D. Brown, D. Altermatt, Bond-valence parameters obtained from a systematic analysis of the Inorganic Crystal Structure Database, Acta. Crystallogr. B., 41 (1985) 244-247.

[67] L.L. Wong, K.C. Phuah, R. Dai, H. Chen, W.S. Chew, S. Adams, Bond Valence Pathway Analyzer—An Automatic Rapid Screening Tool for Fast Ion Conductors within softBV, Chem. Mater., 33 (2021) 625-641.

[68] H. Chen, L.L. Wong, S. Adams, SoftBV - a software tool for screening the materials genome of inorganic fast ion conductors, Acta. Crystallogr. B., 75 (2019) 18-33.

[69] H. Chen, S. Adams, Bond softness sensitive bond-valence parameters for crystal structure plausibility tests, IUCrJ, 4 (2017) 614-625.

[70] H. Fukuda, S. Kusakawa, K. Nakano, N. Tanibata, H. Takeda, M. Nakayama, M. Karasuyama, I. Takeuchi, T. Natori, Y. Ono, Bayesian optimisation with transfer learning for NASICON-type solid electrolytes for all-solid-state Li-metal batteries, RSC Adv., 12 (2022) 30696-30703.

[71] N. Aliahmad, S. Shrestha, K. Varahramyan, M. Agarwal, Poly(vinylidene fluoride-hexafluoropropylene) polymer electrolyte for paper-based and flexible battery applications, AIP Adv., 6 (2016) 065206.

[72] P. M. Shanthi, P. J. Hanumantha, T. Albuquerque, B. Gattu, P.N. Kumta, Novel Composite Polymer Electrolytes of PVdF-HFP Derived by Electrospinning with Enhanced Li-Ion Conductivities for Rechargeable Lithium–Sulfur Batteries, ACS Appl. Energy Mater., 1 (2018) 483.

[73] M. Tripathi, S.M. Bobade, A. Kumar, Preparation of polyvinylidene fluoride-co-hexafluoropropylene-based polymer gel electrolyte and its performance evaluation for application in EDLCs, Bull. Mater. Sci., 42 (2019) 27.

[74] X. Zhang, T. Liu, S. Zhang, X. Huang, B. Xu, Y. Lin, B. Xu, L. Li, C.-W. Nan, Y. Shen, Synergistic Coupling between $Li_{6.75}La_3Zr_{1.75}Ta_{0.25}O_{12}$ and Poly(vinylidene fluoride) Induces

High Ionic Conductivity, Mechanical Strength, and Thermal Stability of Solid Composite Electrolytes, J. Am. Chem. Soc., 139 (2017) 13779-13785.

[75] K. Oumghar, N. Chakhchaoui, R. Farhane, A. Eddiai, M. Meddad, O. Cherkaoui, L. Van Langenhove, Enhanced piezoelectric properties of PVdF-HFP/PZT nanocomposite for energy harvesting application, IOP Conf. Ser.: Mater. Sci. Eng., 827 (2020) 012034.

[76] L.N. Sim, S.R. Majid, A.K. Arof, FTIR studies of PEMA/PVdF-HFP blend polymer electrolyte system incorporated with $LiCF_3SO_3$ salt, Vib. Spectrosc, 58 (2012) 57-66.

[77] W. He, H. Ding, X. Chen, W. Yang, Three-dimensional LLZO/PVDF-HFP fiber network-enhanced ultrathin composite solid electrolyte membrane for dendrite-free solid-state lithium metal batteries, J. Membr. Sci., 665 (2023) 121095.

[78] L. Wu, G. Huang, N. Hu, S. Fu, J. Qiu, Z. Wang, J. Ying, Z. Chen, W. Li, S. Tang, Improvement of the piezoelectric properties of PVDF-HFP using AgNWs, RSC Adv., 4 (2014) 35896-35903.

[79] J. Yin, A. Raegen, S.H.J. Idziak, J.A. Forrest, Crystallization and melting of highly monodisperse poly(ethylene-oxide), Soft Matter, 16 (2020) 7958-7969.

[80] F. Croce, L. Persi, B. Scrosati, F. Serraino-Fiory, E. Plichta, M.A. Hendrickson, Role of the ceramic fillers in enhancing the transport properties of composite polymer electrolytes, Electrochim. Acta, 46 (2001) 2457.

[81] F. Chen, D. Yang, W. Zha, B. Zhu, Y. Zhang, J. Li, Y. Gu, Q. Shen, L. Zhang, D.R. Sadoway, Solid polymer electrolytes incorporating cubic $Li_7La_3Zr_2O_{12}$ for all-solid-state lithium rechargeable batteries, Electrochim. Acta, 258 (2017) 1106.

[82] S.B. Aziz, T.J. Woo, M.F.Z. Kadir, H.M. Ahmed, A conceptual review on polymer electrolytes and ion transport models, J. Sci.: Adv. Mater. Devices, 3 (2018) 1.

[83] Z. Li, H.-M. Huang, J.-K. Zhu, J.-F. Wu, H. Yang, L. Wei, X. Guo, Ionic Conduction in Composite Polymer Electrolytes: Case of PEO:Ga-LLZO Composites, ACS Appl. Mater. Interfaces, 11 (2019) 784-791.

[84] J. Evans, C.A. Vincent, P.G. Bruce, Electrochemical measurement of transference numbers in polymer electrolytes, Polymer, 28 (1987) 2324.

[85] K.-H. Chen, K.N. Wood, E. Kazyak, W.S. LePage, A.L. Davis, A.J. Sanchez, N.P. Dasgupta, Dead lithium: mass transport effects on voltage, capacity, and failure of lithium metal anodes, J. Mater. Chem. A, 5 (2017) 11671-11681.

[86] S. Xia, J. Lopez, C. Liang, Z. Zhang, Z. Bao, Y. Cui, W. Liu, High-Rate and Large-Capacity Lithium Metal Anode Enabled by Volume Conformal and Self-Healable Composite Polymer Electrolyte, Adv. Sci., 6 (2019) 1802353.

[87] Y. Huang, Y. Dong, S. Li, J. Lee, C. Wang, Z. Zhu, W. Xue, Y. Li, J. Li, Lithium Manganese Spinel Cathodes for Lithium-Ion Batteries, Adv. Energy Mater., 11 (2021) 2000997.

Figure captions:

Fig. 3. (a) Powder x-ray diffraction data (open circles) for LZSP sample sintered at 1150 °C for 12 h. The calculated pattern obtained from the refinement is shown as a thick blue line; the

profile difference is depicted with a thin khaki line. The calculated Bragg positions are shown by vertical bars at the bottom, (b) x-ray diffraction patterns of CSE-x (x = 0, 5, 10, 15, and 20).

Fig. 4. (a) Scanning electron microscopy (SEM) image of CSE-15, (b)-(j) Energy dispersive spectroscopy (EDS) data of CSE-15 along with its constituent elemental distributions, (k) Fourier transform infrared spectroscopy of pure P(VDF-HFP) and CSE-x (x = 0, 5, 10, 15, and 20) (Inset Fig. 2(a) shows the photograph of CSE-15 film).

Fig. 3. DSC thermograms of CSE-0 and CSE-15.

Fig. 4. Room temperature Nyquist plots of LZSP ceramics and CSE-x (x = 0, 5, 10, 15, and 20). Fig. 4(a) & 4(b) insets display the equivalent circuits used for fitting the impedance data of LZSP sample & CSE-x (x = 0, 5, 10, 15, and 20).

Fig. 5. Linear fitting using Arrhenius equation for (a) LZSP pellet and (b) CSE-x (x = 0, 5, 10, 15, and 20).

Fig. 6. Cyclic voltammetry on (a) symmetric Li|CSE-15|Li cell and (b) asymmetric Li|CSE-15|SS cell.

Fig. 7. (a)Current variation with time upon applying 0.05 V on symmetric Li|CSE-15|Li cell. The Inset figure shows the Nyquist plots before and after dc polarisation and the equivalent circuit fitted for the calculation of interfacial resistance. (b) Linear sweep voltammetry of CSE-0, CSE-5, CSE-10, CSE-15, and CSE-20.

Fig. 8. Galvanostatic charge-discharge profile of symmetric Li|CSE-15|Li cell.

Fig. 9. (a) Galvanostatic charge-discharge profile of full Li|CSE-15|LMO cell at 0.1 C-rate, (b) differential capacity plot of full Li|CSE-15|LMO at the constant current density of 0.1 mA/cm^2, and (c) galvanostatic charge-discharge profile of full Li|CSE-15|LMO at different C-rates.

[Supplementary Materials]

Highly Conductive Ceramic-in-Polymer Composite Electrolyte Enabling Superior Electrochemical Performance for All-Solid-State Lithium Batteries

Asish Kumar Das, Manish Badole, Hari Narayanan Vasavan, Samriddhi Saxena, Pratiksha Gami, Sunil Kumar*

Department of Metallurgy Engineering and Materials Science, Indian Institute of Technology Indore, Simrol, 453552, India

**Corresponding author E-mail: sunil@iiti.ac.in*

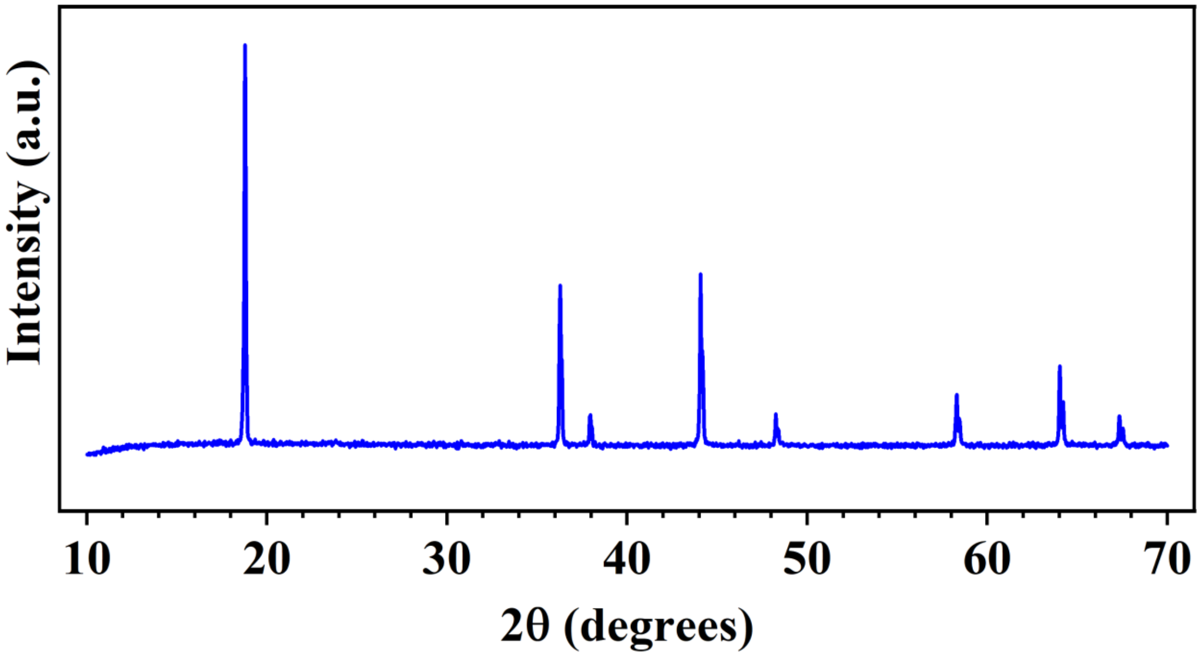

Figure S1: XRD pattern of commercial $LiMn_2O_4$ coated on Aluminum foil.

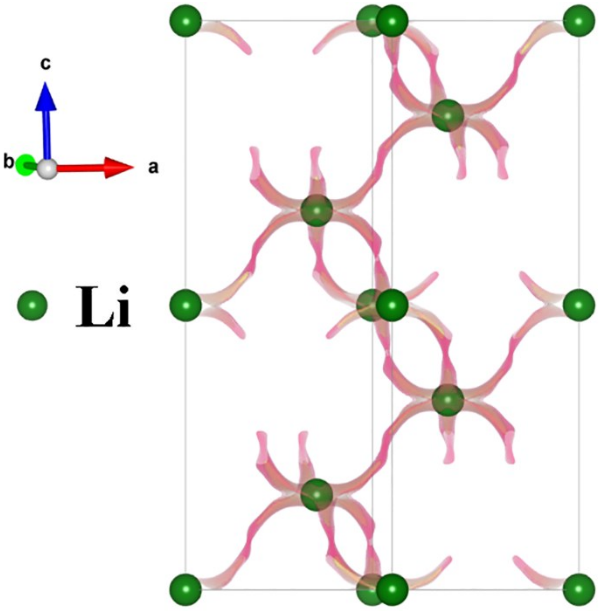

Figure S2 Lithium-ion migration pathways in rhombohedral LZSP crystal (green solid balls represent the lithium atoms).

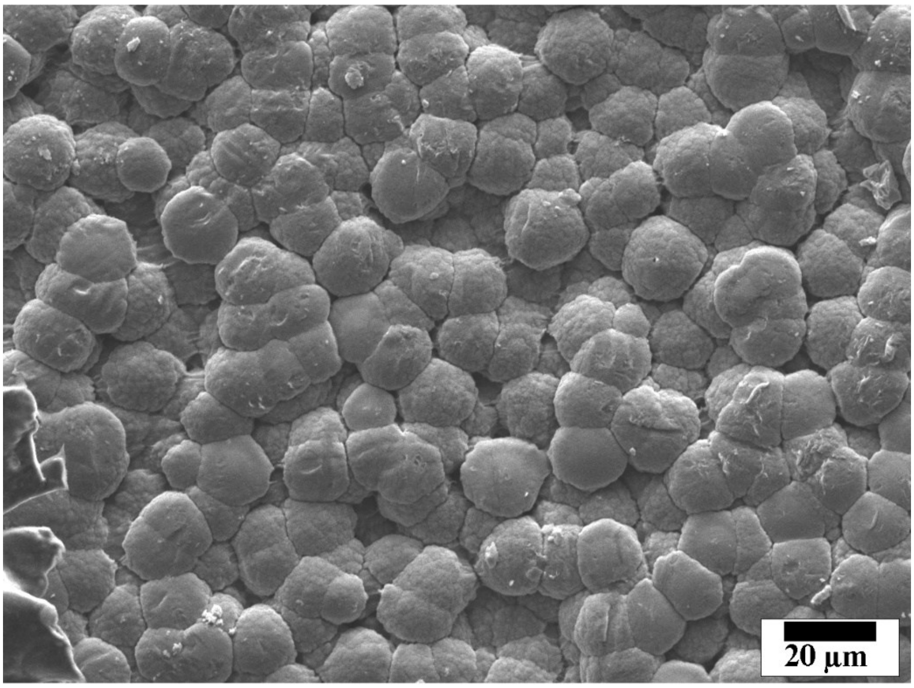

Figure S3: SEM image of CSE-0.

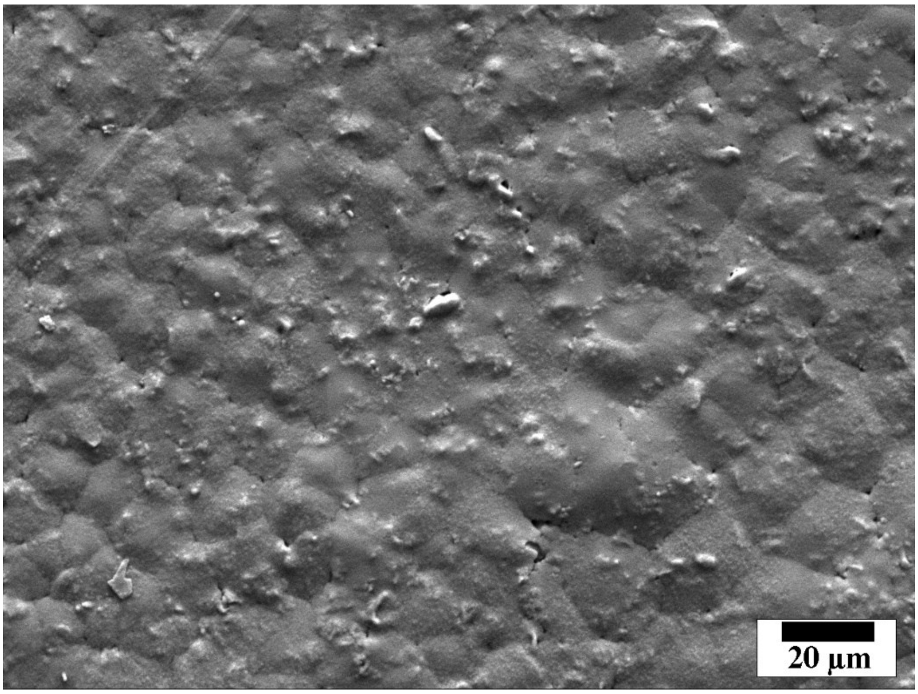

Figure S4: SEM image of CSE-20.

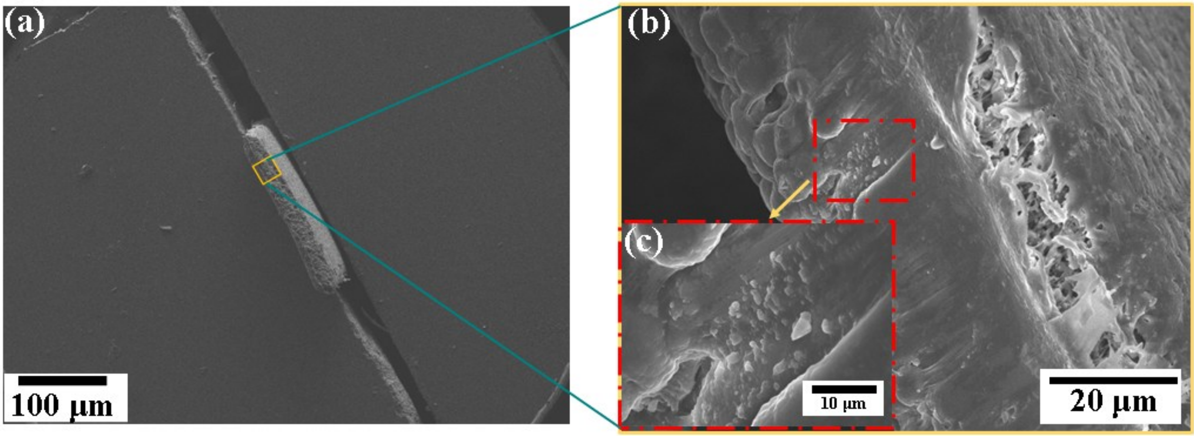

Figure S5: Cross-sectional SEM image of CSE-20.

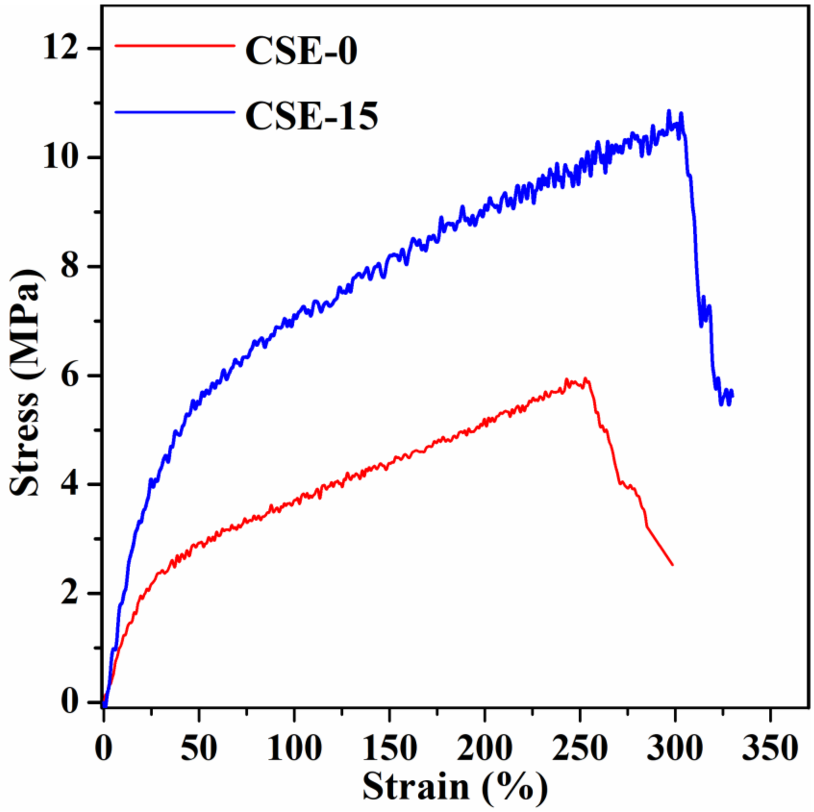

Figure S6: Stress-strain curves of CSE-0 and CSE-15.

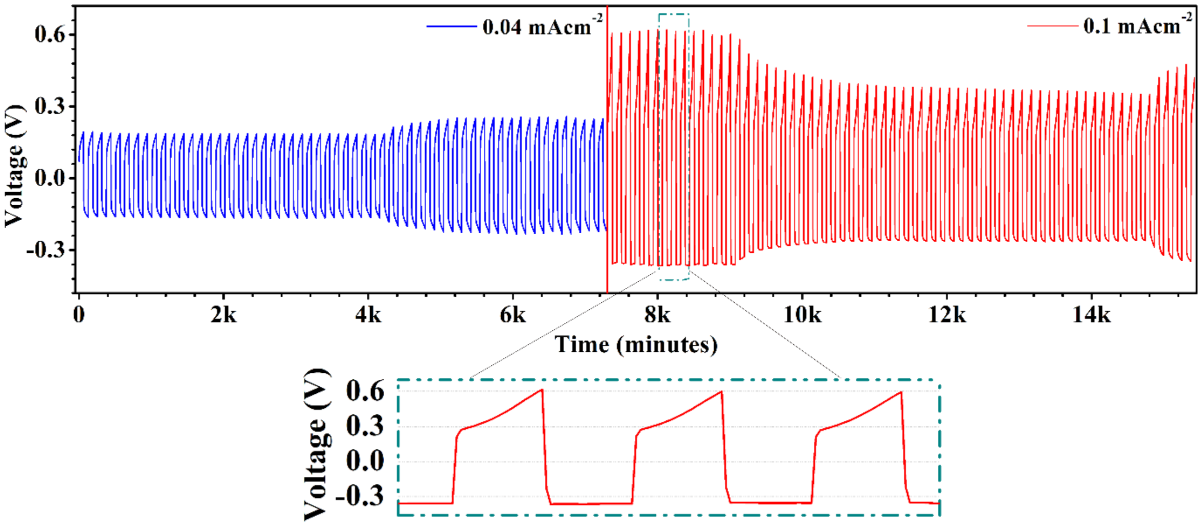

Figure S7: Galvanostatic charge-discharge profile of symmetric Li|CSE-0|Li cell.

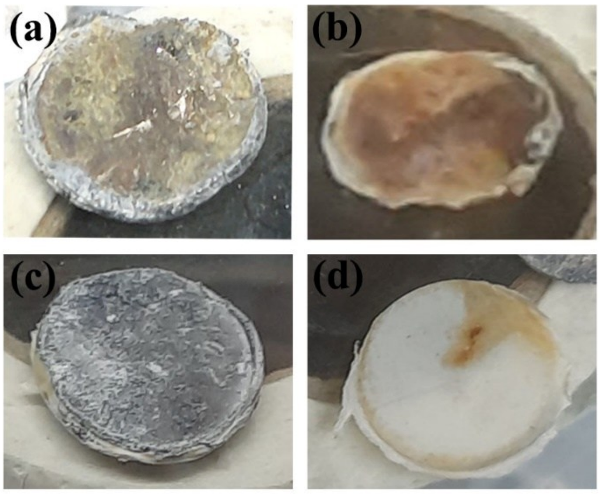

Figure S8: (a) and (b) Lithium metal sheet and CSE-0 harvested from the de-crimped symmetric cell after 100 cycles, respectively. (c) and (d) lithium metal sheet and CSE-15 harvested from the de-crimped symmetric cell after 100 cycles, respectively.